HHS Public Access

Author manuscript

J Surg Res. Author manuscript; available in PMC 2019 March 01.

Published in final edited form as:

J Surg Res. 2018 March ; 223: 115–122. doi:10.1016/j.jss.2017.10.027.

3D Printed Bioactive Ceramic Scaffold Osseoconduction Across Critical-Sized Mandibular Defects

Christopher D. Lopez, BA[1,3,*], **J. Rodrigo Diaz-Siso, MD**[2,*], **Lukasz Witek, MSci, PhD**[3], **Jonathan M. Bekisz, BA**[4], **Bruce N. Cronstein, MD**[5], **Andrea Torroni, MD, PhD**[2], **Roberto L. Flores, MD**[2], **Eduardo D. Rodriguez, MD**[2], and **Paulo G. Coelho, DDS, PhD**[2,3]

[1]Icahn School of Medicine at Mount Sinai, 1 Gustave L. Levy Place, New York NY 10029

[2]Wyss Department of Plastic Surgery, NYU Langone Medical Center, 307 E 33rd St, New York NY 10016

[3]Department of Biomaterials & Biomimetics, NYU College of Dentistry, New York NY, 433 1st Avenue, 8th Floor, New York NY 10010

[4]New York University School of Medicine, 550 1st Avenue, New York NY 10016

[5]Department of Medicine, NYU Langone Medical Center, New York NY, 550 1st Avenue, New York NY 10016

Abstract

Purpose—Vascularized bone tissue transfer, commonly used to reconstruct large mandibular defects, are challenged by long operative times, extended hospital stay, donor-site morbidity, and resulting health care. 3D-printed osteoconductive tissue-engineered scaffolds may provide an alternative solution for reconstruction of significant mandibular defects. This pilot study presents a novel 3D-printed bioactive ceramic scaffold with osteoconductive properties to treat segmental mandibular defects in a rabbit model.

Corresponding author: Paulo G. Coelho, DDS PhD, Leonard I. Linkow Associate Professor, Biomaterials and Biomimetics, NYU College of Dentistry, Wyss Department of Plastic Surgery, NYU Langone Medical Center, 433 1st Ave room 844, New York, NY 10010, Office: 212 998 9214, Pc92@nyu.edu.

*These authors contributed equally to this work.

Author contributions:

Christopher D. Lopez performed all phases of data collection and analysis, including sample preparation via dehydration and embedding, histologic preparation, microCT scanning and 3D reconstruction, and contributed significantly to manuscript preparation. J. Rodrigo Diaz-Siso assisted with conceptualization of this project, assisted with surgical procedure, sample preparation, and manuscript writing. Lukasz Witek designed and created the 3D printed scaffolds, assisted with all aspects of sample preparation, performed statistical analysis, and contributed to manuscript preparation. Jonathan M. Bekisz performed all phases of data collection and analysis, including sample preparation via dehydration and embedding, histologic preparation, microCT scanning and 3D reconstruction, and contributed significantly to manuscript preparation. Bruce N. Cronstein assisted significantly with all aspects of project conceptualization, sample preparation, and manuscript writing. Andrea Torroni contributed to surgical approach and retrieval and significant manuscript writing. Roberto L. Flores contributed to surgical procedure, data analysis and manuscript writing. Eduardo D. Rodriguez contributed to surgical procedure, data analysis, conceptualization of project, and manuscript writing. Finally, Paulo G. Coelho was the primary conceptualizer of this project, contributed to surgical procedure, oversaw all data collection and sample preparation, and contributed extensively to manuscript writing.

Disclosures: The authors report no proprietary or commercial interest in any product mentioned or concept discussed in this article.

Methods—Full-thickness mandibulectomy defects (12mm) were created at the mandibular body of six adult rabbits and replaced by 3D-printed ceramic scaffold made of 100% β-tricalcium phosphate, fit to defect based on CT imaging. After 8-weeks, animals were euthanized, the mandibles were retrieved, and bone regeneration was assessed. Bone growth was qualitatively assessed with histology and backscatter scanning electron microscopy, quantified both histologically and with microCT and advanced 3D image reconstruction software, and compared to unoperated mandible segments (UMS).

Results—Histology quantified scaffold with newly formed bone area occupancy at 54.3 ± 11.7%, compared to UMS baseline bone area occupancy at 55.8 ± 4.4%, and bone area occupancy as a function of scaffold free space at 52.8 ± 13.9%. 3D volume occupancy quantified newly formed bone volume occupancy was 36.3 ± 5.9%, compared to UMS baseline bone volume occupancy at 33.4 ± 3.8%, and bone volume occupancy as a function of scaffold free space at 38.0 ± 15.4%.

Conclusion—3D-printed bioactive ceramic scaffolds can restore critical mandibular segmental defects to levels similar to native bone after 8 weeks in an adult rabbit, critical sized, mandibular defect model.

Keywords

3D printing; tissue engineering; craniomaxillofacial; bone regeneration; reconstruction; osteoconduction

Introduction

Mandibular reconstruction is often required in settings of craniomaxillofacial trauma, congenital disfigurement, and oncologic resection. With the aid of technology, surgeons are able to expedite patient return to baseline function through recent developments in virtual surgical planning (1). Vascularized bone tissue transfer remains the preferred reconstructive option for large mandibular defects, but these flaps are still subject to limitations such as donor site morbidity, prolonged operative time, extended hospital stay, infection, and delayed healing (2–4). In contemporary healthcare, cost must also be considered, as hospital charges for fibula free flaps have been estimated at $60,000 per patient (4). The opportunity to decrease the challenges to free tissue transfer has driven the development of tissue engineering approaches to mandibular reconstruction. Despite the presence of conceptual data in the literature regarding scaffold design parameters and their in vitro osteogenic potential evaluation through various cell culturing methods, there is a paucity of translational *in vivo* studies assessing 3D printed scaffolds (5–7), and an ideal approach to tissue engineered bone repair remains elusive (8).

Within the field of bone tissue engineering, calcium phosphate-based biomaterials have gained prominence due to their osteoconductivity, biocompatibility (9, 10), and reports of safe use for decades (11). Many FDA approved synthetic grafting materials, and bone substitutes, which include calcium phosphate-based bioactive ceramic biomaterials, are utilized in over 50% of bone-grafting cases in the United States (12). Furthermore, applications are limited: while osteoconductive, these materials lack design parameters to

address large, patient-specific defects. Large repair sites require interaction between synthetic grafting material and the defect margins, which is not adequate with granular-based or block-based grafting materials as they cannot be properly shaped to fit and fill defects in a geometrically stable fashion. In addition, though osteoconductive, granular-based graft materials provide nucleation sites for osteogenesis in a random fashion; this lack of spatial coordination hinders organized directional bone growth and extensive subsequent remodeling is necessary for complete repair. Such grafts only provide satisfactory results when packed into defects with bone walls that support bone derived osteogenic content and adequate material packing (e.g. smaller craniomaxillofacial defects). However, little attention has been paid to the geometry of biomaterials and their potential effect on bone regeneration at larger defects, where there is lack of bone derived osteogenic potential, despite modalities such as 3D printing offering an approach to control these parameters.

3D printing of bioactive synthetic materials in scaffold form allows for customized designs based on clinical imaging. 3D printing for tissue engineered bone has been described with varying success over the last fifteen years (13–27), likely due to a lack of hierarchical approach to scaffold design. Geometries at macro- (overall structure), meso- (strut size and pore size/interconnectivity), micro- (surface properties) and nano- (material properties, biocompatibility) structure levels have been individually explored (10, 28), but have lacked multivariable study design, thereby limiting an understanding of the contributions and limitations of each structural level to osteoconductivity. A similar nonhierarchical approach describes a majority of the endosteal implant fixation literature (29), which hindered bioengineers attempting to improve clinical results until a more methodical approach was recently proposed.

Work over the past decade addressed the lack of objective parameter implant studies in order to improve upon biomaterial designs for bone healing (30, 31). This included assessment of factors such as endosteal implant healing chamber dimensions, and how spaces between implant threads interact with violated osteotomy walls to facilitate intramembranous-like healing pathways (31). By methodically assessing these bulk configurations, as well as factors such as surface treatments, endosteal metallic implant work has shed light on design factor contributions to early vs. late bone healing that are likely applicable to biomaterials such as osteoconductive 3D printed scaffolds. Previous studies have highlighted that bioactive ceramic porous geometries demonstrate the same intramembranous-like healing pathway that healing chambers (regions between implant threads) exhibit upon endosteal fixation (31, 32), but are challenged to osteoconduct across large defects instead of small portions of drill sites. Given the variety of bony defects that can require surgical intervention, assessment of macrogeometry at various anatomic sites is warranted to determine where bone can and cannot be regenerated.

The objective of this pilot study is to assess the utility of 3D-printed bioactive ceramic (3DBC) scaffolds for treating significant mandibular defects. We hypothesized that 3DBC scaffolds can successfully repair critical segmental bony defects in a dynamic, load-bearing rabbit mandible.

Materials and Methods

Colloidal Gel formulation

Previously calcined and milled ceramic powders were used for the colloidal gel formulation (33). Concentrated β-TCP colloidal gel, where the solid volume fraction ($\varphi_{ceramics}$) of the ceramic was ~46%, was produced by mixing a pre-calculated amount of ceramic powder, ammonium polyacrylate (~14.5 mg/gram ceramic) (Darvan 821A; RT Vanderbilt, Norwalk, CT, USA) solution to disperse particles, deionized water (DI)-H2O, hydroxypropyl methylcellulose, 7 mg per milliliter of ceramic (Methocel F4M; Dow Chemical Company, Midland, MI, USA) as the thickening agent, and polyethylenimine, 150 to 200 mg per 30 mL of colloidal gel, (Sigma-Aldrich, St. Louis, MO, USA) to gel the colloidal ink suspension (33, 34).

Scaffold Design, Implementation, and Analysis

The β-TCP scaffolds were fabricated via robocasting, using a 3D direct-write micro printer gantry robot system (Aerotech Inc., Pittsburgh, PA, USA) used to extrude the colloidal ink. The 3D defect-sized scaffolds (11-mm length, 9-mm major axis diameter, 4.5mm minor axis diameter; 250 μm struts, and 330 μm pore spacing) were designed with a computer-aided design (CAD) system (RoboCAD 4.3; 3D Inks LLC, Tulsa, OK, USA) to precisely replace defect sites (Figure 1). The colloidal ink was loaded into a syringe (Nordson Corp., Westlake, OH, USA) and subsequently equipped with 250 μm-diameter extrusion nozzle (Nordson Corp.). The 3D cuboidal scaffolds were printed in layer-by-layer fashion at 8-mm/s print speed. The entire deposition process occurred in a low-viscosity paraffin oil tray to prevent drying of the structure during fabrication. After being allowed to partially dry, scaffolds were sintered in a multi-step process which ending with a dwell at 1100°C for 4hrs; higher temperature (1100°C) allowed for construct densification (34) while two lower temperature dwells (400°C and 900°C) allowed for organic burnout.

In Vivo Rabbit Model Surgical Procedure

Following approval of Institutional Animal Care and Use Committee, all surgeries were performed under sterile conditions. Following pre-treatment with subcutaneous buprenorphine (0.02 mg/kg) and enrofloxacin (5 mg/kg), five rabbits were anesthetized via intramuscular administration of Ketamine (35 mg/kg) and Xylazine (5mg/kg). Through a 5-cm submandibular incision, a 12mm segmental defect was created at the mandibular body in five skeletally mature New Zealand White rabbits (NZWRs), weighing ~3.5kg (Figure 2A and 2B). One scaffold was inserted into each (Figure 2B) defect and plated (Signo-Vinces, Campo Largo, Brazil) in continuity with bone, then overlying soft tissue and skin were closed; no evidence of oral cavity communication occurred. Each animal's contralateral mandibular body served as its own uninjured internal control. Buprenorphine (0.01 mg/kg) and enrofloxacin (5 mg/kg) were administered every 12 hours for 48 hours post-op. Animals were given food *ad libitum*, without activity restrictions, and were euthanized via anesthetic overdose at 8-weeks.

Advanced Imaging and 3D Quantification

Samples were scanned using micro-computed tomography (μCT 40, Scanco Medical, Basserdorf, Germany). All DICOM format data were imported into Amira 6.1 software (Visage Imaging GmbH, Berlin, Germany) for quantitative analysis of bone formation. Scaffold was isolated via volume editing, and regions of bone were isolated by thresholding. Bone was quantified using Amira 6.1 software material statistics.

Histologic Preparation, Scanning Electron Microscopy, 3D Quantification and Statistical Analysis

After scanning, the embedded blocks were cut into sections using a diamond saw (Isomet 2000, Buehler Ltd., Lake Bluff, IL, USA). The sections were ground on a grinding machine (Metaserv 3000, Buehler, Lake Bluff, IL, USA) under water irrigation with a series of SiC abrasive paper until they were ~100 μm thick, after which samples were stained in Stevenel's blue and Van Geison red to differentiate the soft, connective, and bony tissues. Qualitative depictions of bone regeneration were performed using histology and corresponding regions with backscatter electron microscopy. Histological and 3D reconstructed data are presented as mean values with 95% confidence interval (CI). To accurately report new bone growth, unoperated mandible sections (UMS) from the contralateral mandibular body underwent 2D and 3D analysis to quantify native bone area and volume occupancy for comparisons with scaffold regenerated segments.

All %bone data were analyzed using paired t-test with a confidence interval of 95% (IBM SPSS v23, IBM Corp., Armonk, NY, USA).

Results

Two animals presented signs of infection approximately ten days after surgery. While both animals successfully completed the study time frame, necropsy revealed lack of scaffold osseointegration and these samples were excluded from analyses. Removal of surgical hardware for the remaining subjects revealed scaffold integration (Figure 3A). 3D analysis demonstrated directional bony ingrowth from both defect walls into scaffold pores and lumen (Figure 3B and 3C). Histomorphologic assessment depicted no inflammation, and bone healing by an intramembranous-like healing pathway, bridging both bone segments within the scaffold. A highly cellular and vascularized woven bone structure was observed in direct contact with the scaffold, within the scaffold structure, and within the scaffold lumen (Figure 4A). High magnification depicted contact between woven bone and a resorbing scaffold structure, as well as regions of lamellar bone formation surrounding primary osteonic structures with vascular components at their respective centers within the scaffold porosity (Figure 4B and 4C). Scanning electron microscopy depicts bone healing with a spectrum of bone maturity ranging from woven to lamellar reorganization, with scaffold strut resorption (Figure 5), as well as concentric rings forming, guided/directional new bone formation between struts, bone-mediated scaffold resorption at bone/scaffold interfaces, and microcracks corresponding to regions of bone remodeling (Figure 6A).

Histology quantified bone area occupancy as a function of scaffold free space at 52.83 ± 13.93%. 2D quantity of scaffold with newly formed bone was not statistically different from UMS bone area occupancy (54.39 ± 11.76% and 55.8 ± 4.4%, respectively, p=0.85) (Figure 7A–C). 3D analysis quantified bone volume occupancy as a function of free space at 38.01 ± 15.18%. 3D scaffold with newly formed bone volume occupancy was not statistically different from UMS bone volume occupancy (36.33 ± 5.96% and 33.4 ± 3.8%, respectively, p=0.32) (Figure 7A–C).

Discussion

The promise of biomaterial synthesis and tissue engineering has yet to be realized, yet the principles of bone healing have been well-described in biomaterials such as endosteal implants and other implantable scaffolds; osseointegration via rapid, new bone formation has been widely reported. This pilot study explored mandibular regeneration by using 3D printing to synthesize β-TCP scaffolds with porous geometries that augment osteoconduction in healing chambers of metallic biomaterials and lattice-based scaffolds at critical-size defects.

The scaffold strut and porous dimensions used in this study were designed to elicit bone healing behavior reminiscent of osseointegration, the intimate contact between living bone and endosteal implant (31). Scaffold pores behaved as healing chambers, guiding osteoconduction where surgically violated bone walls ossified directionally into pores via an intramembranous-like healing pathway quickly filling the scaffold lattice structure with woven bone (31). Continuous communication of pores across the entire scaffold was critical, as reports have unequivocally described dimensional limits for optimal healing chamber configurations to hasten bone formation (35). Scaffold porosity has been suggested to be permissive to factors that facilitate bone healing (e.g. blood clot rich in osteogenic cells) (29).

The critical-size defect in this study exceeded established protocol dimensions (36). Full-thickness circular defects 10mm in diameter have been established as critical-sized in the rabbit mandible (36), even with mandible continuity at the superior and inferior margins. Our defect was 12mm in length and required plating as mandible continuity was completely interrupted. The porous β-TCP scaffolds conducted bone regeneration bridging this defect span through initial extensive woven bone formation despite atemporal return to masticatory function employed in the current model. At the 8-week in vivo endpoint, initial woven bone replacement with lamellar bone was observed along with scaffold resorption. Historically, scaffold designs have been comprised of hydroxyapatite (HA) as bulk material. HA has been blended and 3D printed with polymers such as Polycaprolactone (PCL) and Polylactic Acid (PLA) (37); PCL and PLA are biodegradable, biocompatible polyesters, but are not ideal for bone tissue engineering due to inferior mechanical properties (e.g. compressive strength, Young's modulus) (37) and questionable osteoconductive capacity (38), both of which are addressed by the properties of HA (37). However, relative to β-TCP, HA has a high initial compressive strength and low resorption kinetics *in vivo* (1–2% per year at five years post-implantation) (39), thus limiting temporal scaffold material replacement by bone. β-TCP as a bioactive ceramic material has been demonstrated to degrade/resorb more rapidly *in vitro*

and *in vivo* relative to HA, allowing for more rapid bone replacement. From a lattice-based scaffold designing standpoint, this material degradation rate can be altered by increasing the scaffold macroscopic surface area via strut diameter changes (struts of a smaller diameter result in higher surface area) or by changing material micro/nano porosity levels through the interplay of ink formulation and sintering processes.

Our results were presented as scaffold + bone occupancy of defect site relative to UMS dimensions and UMS bone occupancy. They were reported together because as β-TCP resorbs, new bone formation replaces it; β-TCP's rapid resorption kinetics were exploited to potentially achieve total scaffold replacement by bone over time. New bone + β-TCP scaffold occupancy at 8 weeks was comparable to UMS bone occupancy at skeletal maturity, irrespective of two or three-dimensional analysis. Bone alone accounted for up to half of this occupancy. Histology and scanning electron microscopy both demonstrated directional bony ingrowth into the scaffold interstices, tracking healing pathway origins to defect walls and marrow spaces. Electron microscopy revealed both new bone growth and scaffold resorption at bone/scaffold interfaces. While bony healing within 3DBC scaffolds has been reported in *in vivo* models (10), a significant bone healing response of a critical segmental defect in a weight bearing mandible has not been reported to date.

Favorable results were observed in the present study by utilizing principles of biomaterial design to regenerate bone without bioactive molecule enhancement. This approach has been taken by other groups (10), but to our knowledge, not in a mandible model. Others have addressed bone regeneration through cellular (stem cell seeding) and molecular (bone morphogenetic protein signaling) mechanisms (40, 41). Their results have offered insight on the osseoinductive pathway of mesenchymal stem cells and proven that 3D printing can direct spatial control of osteoblast differentiation based on design and deposition of growth factors/inhibitors. However, stem cell therapy has yet to demonstrate regenerative outcomes of clinical interest and continue to be strictly regulated and present ethical dilemmas. Our focus on biomaterial properties did not require supplements to augment local cellular nourishment/healing pathways, utilized endogenous healing mechanisms, and required less time and variables to achieve a clinical outcome associated with stem cell harvest, culturing, scaffold seeding, growth within a bioreactor and implantation. Another study employing the same scaffold lattice parameters and material used in the present investigation, when coated with an adenosine A2 receptor ($A_{2A}R$) indirect agonist, demonstrated augmented bone growth in a murine calvarial model as effectively as rhBMP-2 (42), without the complications of BMPs (e.g. exuberant bone formation) (43). These positive results with respect to increased bone formation capacity through the addition of $A_{2A}R$ indirect agonism, to devices of the same mesoscale geometry and material utilized in the present study, indicate that exploration of $A_{2A}R$ activation efficacy with osteoconductive scaffolds at critical segmental mandible models are warranted. Longer time frame studies in more challenging settings (e.g. soft tissue deficit) should also be assessed to determine if bone growth will adequately replace the resorbable scaffold and restore full function and shape of the resected mandible. The replacement of free space with new bone will likely vary as scaffolds resorb over time, thus also citing a need for a longer time frame to determine when full scaffold resorption is achieved. Studies addressing these gaps of knowledge pertaining to regenerative capacity and degree of scaffold resorption with and without $A_{2A}R$ coating

are underway in translational models of the mandibular ramus, upper extremity, calvaria and alveolar process.

Acknowledgments

Funding: This work was supported by the National Institute of Arthritis and Musculoskeletal and Skin Diseases [award 5R01AR068593-02 and award supplement 3R01AR068593-02S1].

References Cited

1. Levine JP, Bae JS, Soares M, Brecht LE, Saadeh PB, et al. Jaw in a day: total maxillofacial reconstruction using digital technology. Plastic and Reconstructive Surgery. 2013; 131:1386–1391. [PubMed: 23714799]
2. Hidalgo DA. Condyle transplantation in free flap mandible reconstruction. Plastic and reconstructive surgery. 1994; 93:770–781. [PubMed: 8134436]
3. Hidalgo DA, Rekow A. A review of 60 consecutive fibula free flap mandible reconstructions. Plastic and reconstructive surgery. 1995; 96:585–596. [PubMed: 7638283]
4. Hultman CS. Procedural Portfolio Planning in Plastic Surgery, Part 2: Collaboration Between Surgeons and Hospital Administrators to Develop a Funds Flow Model for Procedures Performed at an Academic Medical Center. Annals of Plastic Surgery. 2016; 76:S347–S351. [PubMed: 27187254]
5. Temple JP, Hutton DL, Hung BP, Huri PY, Cook CA, et al. Engineering anatomically shaped vascularized bone grafts with hASCs and 3D-printed PCL scaffolds. Journal of biomedical materials research Part A. 2014; 102:4317–4325. [PubMed: 24510413]
6. Bose S, Tarafder S, Bandyopadhyay A. Effect of Chemistry on Osteogenesis and Angiogenesis Towards Bone Tissue Engineering Using 3D Printed Scaffolds. Annals of Biomedical Engineering. 2016:1–12. [PubMed: 26620776]
7. Zhang W, Lian Q, Li D, Wang K, Hao D, et al. Cartilage repair and subchondral bone migration using 3D printing osteochondral composites: a one-year-period study in rabbit trochlea. BioMed research international. 2014; 2014
8. Kinoshita Y, Maeda H. Recent developments of functional scaffolds for craniomaxillofacial bone tissue engineering applications. The Scientific World Journal. 2013; 2013
9. Inzana JA, Olvera D, Fuller SM, Kelly JP, Graeve OA, et al. 3D printing of composite calcium phosphate and collagen scaffolds for bone regeneration. Biomaterials. 2014; 35:4026–4034. [PubMed: 24529628]
10. Simon JL, Michna S, Lewis JA, Rekow DE, Thompson VP, et al. In vivo bone response to 3D periodic hydroxyapatite scaffolds assembled by direct ink writing. Journal of Biomedical Materials Research Part A. 2007; 83A:747–758.
11. Nicholas RW, Lange TA. Granular tricalcium phosphate grafting of cavitary lesions in human bone. Clinical orthopaedics and related research. 1994; 306:197–203.
12. Roberts TT, Rosenbaum AJ. Bone grafts, bone substitutes and orthobiologics: the bridge between basic science and clinical advancements in fracture healing. Organogenesis. 2012; 8:114–124. [PubMed: 23247591]
13. Seitz H, Rieder W, Irsen S, Leukers B, Tille C. Three-dimensional printing of porous ceramic scaffolds for bone tissue engineering. Journal of Biomedical Materials Research Part B: Applied Biomaterials. 2005; 74:782–788.
14. Cai S, Xi J, Chua CK. A novel bone scaffold design approach based on shape function and all-hexahedral mesh refinement. Computer-Aided Tissue Engineering. 2012:45–55.
15. Castilho M, Dias M, Gbureck U, Groll J, Fernandes P, et al. Fabrication of computationally designed scaffolds by low temperature 3D printing. Biofabrication. 2013; 5:035012. [PubMed: 23887064]
16. Wang X, Schröder HC, Müller WE. Enzymatically synthesized inorganic polymers as morphogenetically active bone scaffolds: application in regenerative medicine. Int Rev Cell Mol Biol. 2014; 313:27–77. [PubMed: 25376489]

17. Zhou Z, Buchanan F, Mitchell C, Dunne N. Printability of calcium phosphate: calcium sulfate powders for the application of tissue engineered bone scaffolds using the 3D printing technique. Materials Science and Engineering: C. 2014; 38:1–10. [PubMed: 24656346]
18. Farzadi A, Solati-Hashjin M, Asadi-Eydivand M, Osman NAA. Effect of layer thickness and printing orientation on mechanical properties and dimensional accuracy of 3D printed porous samples for bone tissue engineering. PloS one. 2014; 9:e108252. [PubMed: 25233468]
19. Yao Q, Wei B, Guo Y, Jin C, Du X, et al. Design, construction and mechanical testing of digital 3D anatomical data-based PCL–HA bone tissue engineering scaffold. Journal of Materials Science: Materials in Medicine. 2015; 26:1–9.
20. Cox SC, Thornby JA, Gibbons GJ, Williams MA, Mallick KK. 3D printing of porous hydroxyapatite scaffolds intended for use in bone tissue engineering applications. Materials Science and Engineering: C. 2015; 47:237–247. [PubMed: 25492194]
21. Hollister SJ, Flanagan CL, Zopf DA, Morrison RJ, Nasser H, et al. Design control for clinical translation of 3D printed modular scaffolds. Annals of biomedical engineering. 2015; 43:774–786. [PubMed: 25666115]
22. Luo Y, Zhai D, Huan Z, Zhu H, Xia L, et al. Three-dimensional printing of hollow-struts-packed bioceramic scaffolds for bone regeneration. ACS applied materials & interfaces. 2015; 7:24377–24383. [PubMed: 26479454]
23. Brunello G, Sivolella S, Meneghello R, Ferroni L, Gardin C, et al. Powder-based 3D printing for bone tissue engineering. Biotechnology advances. 2016
24. Xinning Y, Jinghua F, Jianyang L, Xianyan Y, Dongshuang H, et al. Fabrication of bioactive tissue engineering scaffold for reconstructing calcified cartilage layer based on three-dimension printing technique. Zhejiang da xue xue bao Yi xue ban= Journal of Zhejiang University Medical sciences. 2016; 45:126–131. [PubMed: 27273985]
25. Cooke MN, Fisher JP, Dean D, Rimnac C, Mikos AG. Use of stereolithography to manufacture critical-sized 3D biodegradable scaffolds for bone ingrowth. Journal of Biomedical Materials Research Part B: Applied Biomaterials. 2003; 64:65–69. [PubMed: 12516080]
26. Gonçalves EM, Oliveira FJ, Silva RF, Neto MA, Fernandes MH, et al. Three-dimensional printed PCL-hydroxyapatite scaffolds filled with CNTs for bone cell growth stimulation. Journal of Biomedical Materials Research Part B: Applied Biomaterials. 2015
27. Provaggi E, Leong JJ, Kalaskar DM. Applications of 3D printing in the management of severe spinal conditions. Proceedings of the Institution of Mechanical Engineers, Part H: Journal of Engineering in Medicine. 2016 0954411916667761.
28. Wilson CE, de Bruijn JD, van Blitterswijk CA, Verbout AJ, Dhert WJA. Design and fabrication of standardized hydroxyapatite scaffolds with a defined macro-architecture by rapid prototyping for bone-tissue-engineering research. Journal of Biomedical Materials Research Part A. 2004; 68A: 123–132.
29. Coelho PG, Jimbo R, Tovar N, Bonfante EA. Osseointegration: Hierarchical designing encompassing the macrometer, micrometer, and nanometer length scales. Dental Materials. 2015; 31:37–52. [PubMed: 25467952]
30. Coelho PG, Granato R, Marin C, Teixeira HS, Suzuki M, et al. The effect of different implant macrogeometries and surface treatment in early biomechanical fixation: an experimental study in dogs. Journal of the mechanical behavior of biomedical materials. 2011; 4:1974–1981. [PubMed: 22098896]
31. Coelho PG, Jimbo R. Osseointegration of metallic devices: current trends based on implant hardware design. Archives of biochemistry and biophysics. 2014; 561:99–108. [PubMed: 25010447]
32. Liao HT, Lee MY, Tsai WW, Wang HC, Lu WC. Osteogenesis of adipose-derived stem cells on polycaprolactone–β-tricalcium phosphate scaffold fabricated via selective laser sintering and surface coating with collagen type I. Journal of Tissue Engineering and Regenerative Medicine. 2016; 10:E337–E353. [PubMed: 23955935]
33. Witek L, Smay J, Silva NR, Guda T, Ong JL, et al. Sintering effects on chemical and physical properties of bioactive ceramics. Journal of Advanced Ceramics. 2013; 2:274–284.

34. Szpalski C, Nguyen PD, Vasiliu CEC, Chesnoiu-Matei I, Ricci JL, et al. Bony engineering using time-release porous scaffolds to provide sustained growth factor delivery. Journal of Craniofacial Surgery. 2012; 23:638–644. [PubMed: 22565873]

35. Marin C, Granato R, Suzuki M, Gil JN, Janal MN, et al. Histomorphologic and histomorphometric evaluation of various endosseous implant healing chamber configurations at early implantation times: a study in dogs. Clinical oral implants research. 2010; 21:577–583. [PubMed: 20105196]

36. Shah SR, Young S, Goldman JL, Jansen JA, Wong ME, et al. A composite critical-size rabbit mandibular defect for evaluation of craniofacial tissue regeneration. Nature Protocols. 2016; 11:1989–2009. [PubMed: 27658014]

37. Sheikh Z, Najeeb S, Khurshid Z, Verma V, Rashid H, et al. Biodegradable materials for bone repair and tissue engineering applications. Materials. 2015; 8:5744–5794. [PubMed: 28793533]

38. Luvizuto ER, Queiroz TP, Margonar R, Panzarini SR, Hochuli-Vieira E, et al. Osteoconductive Properties of β-Tricalcium Phosphate Matrix, Polylactic and Polyglycolic Acid Gel, and Calcium Phosphate Cement in Bone Defects. Journal of Craniofacial Surgery. 2012:23.

39. Moore WR, Graves SE, Bain GI. Synthetic bone graft substitutes. ANZ J Surg. 2001; 71:354–361. [PubMed: 11409021]

40. Weinand C, Neville CM, Weinberg E, Tabata Y, Vacanti JP. Optimizing Biomaterials for Tissue Engineering Human Bone Using Mesenchymal Stem Cells. Plastic and reconstructive surgery. 2016; 137:854–863. [PubMed: 26910665]

41. Cooper GM, Miller ED, DeCesare GE, Usas A, Lensie EL, et al. Inkjet-based biopatterning of bone morphogenetic protein-2 to spatially control calvarial bone formation. Tissue Engineering Part A. 2010; 16:1749–1759. [PubMed: 20028232]

42. Mediero A, Wilder T, Reddy VS, Cheng Q, Tovar N, et al. Ticagrelor regulates osteoblast and osteoclast function and promotes bone formation in vivo via an adenosine-dependent mechanism. The FASEB Journal. 2016; 30:3887–3900. [PubMed: 27511945]

43. Kinsella CR Jr, Cray JJ, Durham EL, Burrows AM, Vecchione L, et al. Recombinant Human Bone Morphogenetic Protein-2–Induced Craniosynostosis and Growth Restriction in the Immature Skeleton. Plastic and reconstructive surgery. 2011; 127:1173–1181. [PubMed: 21364420]

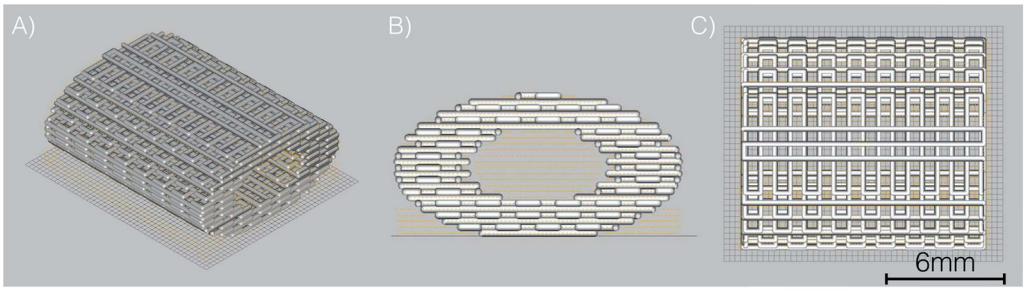

Figure 1.
CAD Scaffold 12mm length, 9mm outer diameter, 5mm inner diameter (lumen),1.95 aspect ratio (a) Iso view (b) front view and (c) superior view

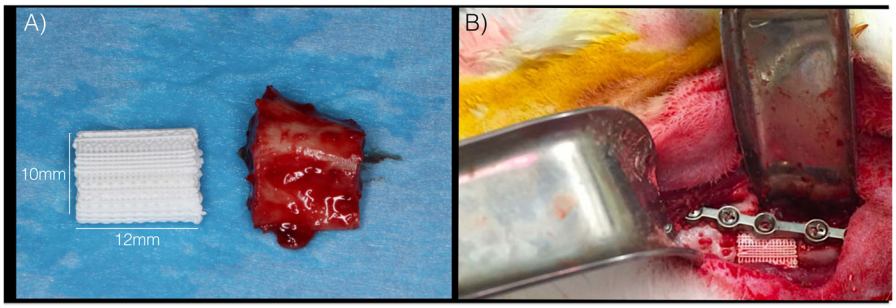

Figure 2.
Scaffold Placement (a) surgical segment compared to scaffold (b) surgical placement of scaffold

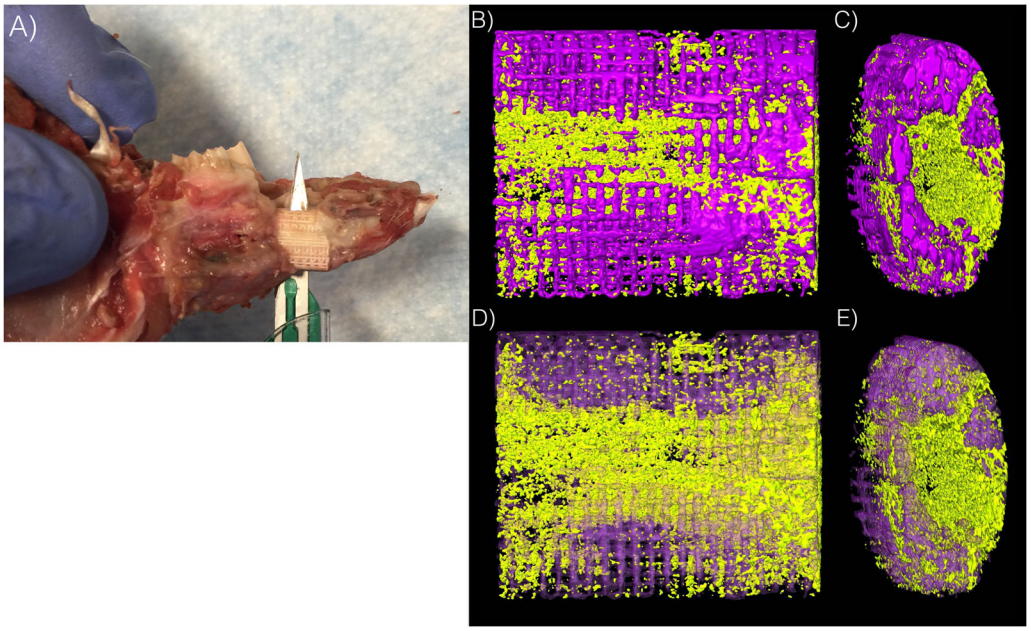

Figure 3.

(a) scaffold integration with rabbit mandible (b) lengthwise 3D reconstruction of scaffold (c) end of scaffold with bony infiltration of lumen (d) lengthwise 3D reconstruction of scaffold with translucent scaffold, solid bone (e) end of scaffold with bony infiltration of lumen with translucent scaffold, solid bone **scaffold in purple, bone in yellow*

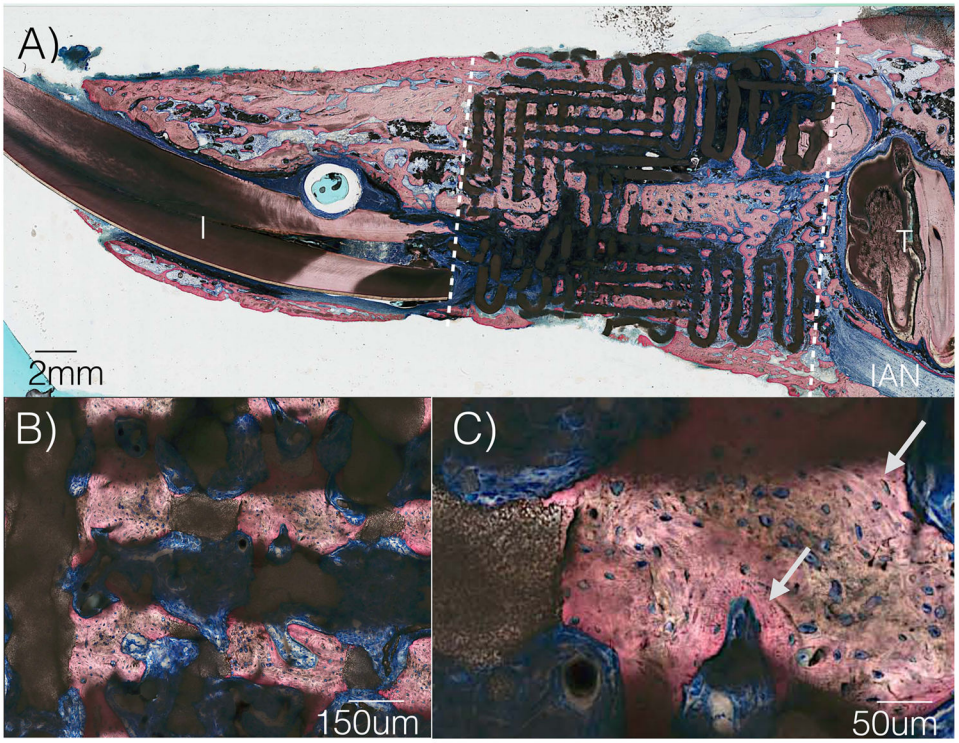

Figure 4.

(a) Sagittal histologic slice of scaffold in continuity with rabbit mandible (b) High magnification from 4a demonstrating porous ingrowth (c) Highly cellular and vascularized woven bone structure, as well as newer, organized lamellar bone formation depicted by arrows. (I=Incisor, T= tooth, IAN= inferior alveolar nerve)

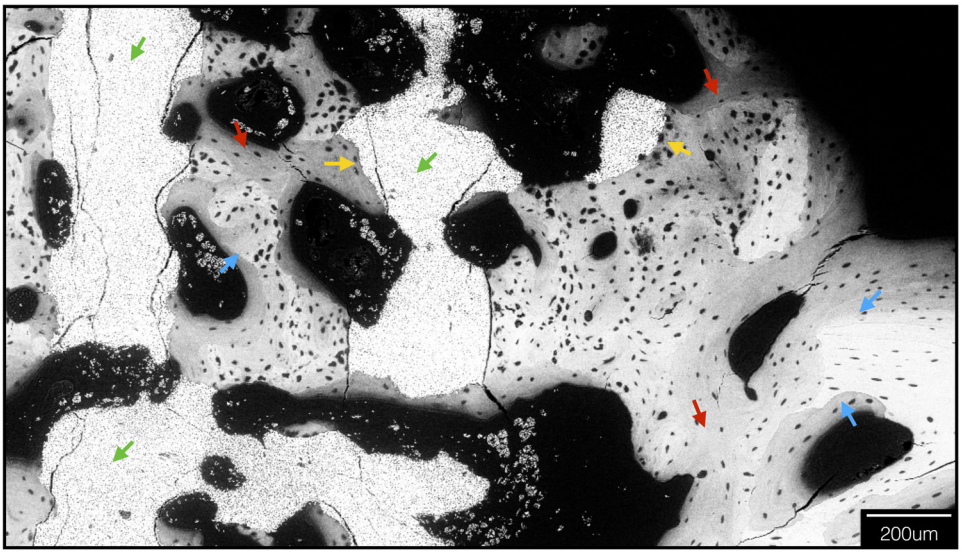

Figure 5.

Electron microscopy depicting scaffold struts (green arrows) and new, intramembranous like bone formation throughout scaffold interstices (red arrows). New, woven bone is seen filling sites of scaffold degradation (yellow arrows), and regions of lamellar reorganization juxtaposed with immature woven bone are evident (blue arrows, lamellar as brighter bone, woven is darker).

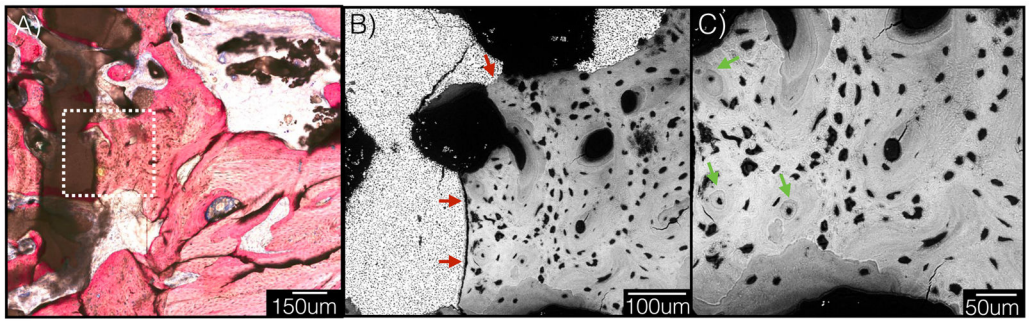

Figure 6.

(a) new bone formation on optical micrograph, with region selected for electron microscopy outlined (b) Bone/scaffold interface depiction with electron microscopy (red arrows) (c) Osteon depicted with concentric rings (green arrows) with electron microscopy

Figure 7.

(a) UMS bone area occupancy vs. scaffold + bone area occupancy at 8 weeks (b) UMS bone volume occupancy vs. scaffold + bone volume occupancy at 8 weeks (c) Bone occupancy within scaffold free space (n=5 rabbits).